

# Geomechanical analysis of microseismicity in an organic shale: A West Virginia Marcellus Shale example

Erich Zorn<sup>1</sup>, Abhash Kumar<sup>2</sup>, William Harbert<sup>3</sup>, and Richard Hammack<sup>4</sup>

## Abstract

Using an innovative workflow incorporating microseismic attributes and geomechanical well logs, we have defined major geomechanical drivers of microseismic expression to understand reservoir stimulation response in an engineering/geologic context. We sampled microseismic data from two hydraulically fractured Marcellus wells in the Appalachian Basin, West Virginia, vertically through the event cloud, crossing shale, limestone, sandstone, and chert. We focused our analysis on the Devonian organic shale and created pseudologs of moment magnitude  $M_w$ ,  $b$ -value, and event count. The vertical moving-average sampling of microseismic data was completed such that the sample interval matched that of the geophysical well log. This technique creates robust, high-resolution microseismic logs that indicate subtle changes in microseismic properties and allow direct crossplotting of microseismic versus geophysical logs. We chose five geomechanical properties to form the framework against which to interrogate the microseismic data: Young's modulus (YM), Poisson's ratio (PR), brittleness,  $\lambda$ -rho, and  $\mu$ -rho. In addition, we included gamma as a useful measure of organic content. Having defined this microseismic-geomechanical crossplot space, we derived insights into the response of these units during hydraulic fracturing. Observations include (1) larger magnitude microseismicity occurs in high PR, high YM rocks; high event counts are found in low PR rocks, (2) low  $b$ -value (high in situ stress) is consistent with the occurrence of larger magnitude events and low event counts, and (3) YM and PR act as bounding conditions, creating "sweet spots" for high and low  $M_w$ , event count, and stress. In our crossplot space, there is a meaningful link between microseismicity and the elastic properties of the host rock. In light of this dependence of stimulation potential on elastic properties, the calculation of microseismic pseudologs at stimulation sites and application of our crossplot framework for microseismic-geomechanical analysis in unconventional shale will inform operators in planning and forecasting stimulation and production, respectively.

## Introduction

In late 2015, two parallel horizontal wells at the Marcellus Shale Energy and Environmental Laboratory (MSEEL) site in Monongalia County, West Virginia, were drilled and hydraulically fractured in the Marcellus Shale over 58 stages (Figure 1). The wells were stimulated separately from each other, with the more northerly well (well 5) completed first, then the southerly well (well 3) second, as opposed to a "zipper-frac" or simulfrac. Microseismic monitoring was completed by Schlumberger, deploying one 12-level (100 ft spacing) Versatile Seismic Imager (VSI) array down one

vertical deep well (pilot well). In addition, standard well logs such as p-sonic, s-sonic, bulk density, total porosity, and natural gamma were acquired in the pilot well, and a full suite of geomechanical well logs was acquired along the length of one of the horizontal wells.

In this study, 25,116 microseismic events were recorded at the geophones over the course of 52 out of the 58 stages of treatment, ranging between moment magnitude  $M_w$   $-3.15$  and  $-0.05$ , with a mean value of  $M_w$   $-2.14$ . The seismogenic  $b$ -value (hereafter, referred to as the  $b$ -value) is the slope of the linear portion of the  $\log_{10}$  (frequency) versus magnitude distribution

<sup>1</sup>Formerly Oak Ridge Institute for Science and Education, National Energy Technology Laboratory, United States Department of Energy, Pittsburgh, Pennsylvania, USA; presently DiGioia Gray and Associates, Pittsburgh, Pennsylvania, USA. E-mail: erich.zorn@gmail.com.

<sup>2</sup>National Energy Technology Laboratory, United States Department of Energy, Pittsburgh, Pennsylvania, USA. E-mail: abhash.kumar@netl.doe.gov.

<sup>3</sup>Oak Ridge Institute for Science and Education, National Energy Technology Laboratory, United States Department of Energy, Pittsburgh, Pennsylvania, USA and University of Pittsburgh, Department of Geology and Environmental Science, Pittsburgh, Pennsylvania, USA. E-mail: william.harbert@contr.netl.doe.gov.

<sup>4</sup>National Energy Technology Laboratory, United States Department of Energy, Water and Energy Team, Pittsburgh, Pennsylvania, USA. E-mail: richard.hammack@netl.doe.gov.

Manuscript received by the Editor 26 March 2018; revised manuscript received 22 July 2018; published ahead of production 12 November 2018; published online 23 January 2019. This paper appears in *Interpretation*, Vol. 7, No. 1 (February 2019); p. T231–T239, 11 FIGS.

<http://dx.doi.org/10.1190/INT-2018-0072.1>. © 2019 Society of Exploration Geophysicists and American Association of Petroleum Geologists. All rights reserved.

in a seismic catalog, and it is an indicator of in situ stress conditions. We used the seismological toolset ZMAP (Wiemer, 2001). The magnitude of completeness  $M_c$  is the minimum magnitude above which the distribution still follows the Gutenberg-Richter power law relationship. The value of  $M_c$  for this data set varies between  $-1.8$  and  $-2.2$  depending upon the method of calculation. The value of  $M_c$  can be calculated by modeling the catalog for the entire magnitude range (EMR) and determining the point at which the distribution becomes nonlinear or nonself-similar; this is known as the EMR method (Woessner, 2005). A simpler method is to find the point of maximum curvature (MaxC) in the frequency-magnitude distribution. The overall  $b$ -value for the entire catalog from both wells ranges between 1.2 and 1.5, depending upon the  $M_c$  calculated (Figure 2a). Because well 5 was stimulated completely before well 3, this completion presented an opportunity to evaluate differences between the characteristics of microseismicity in ambient stress conditions (well 5) and asymmetrically prestressed conditions (well 3). The  $b$ -value of the well 5 microseismic catalog is between 1.1 and 1.4, and the  $b$ -value for well 3 is 1.3–1.7 (Figure 2b and 2c). Figure 2d shows the spatial distribution of  $b$ -values in map view, and we saw a general indication of lower  $b$ -values along well 5 than along well 3. This difference indicates some change in the state of stress because of the stimulation of well 5. Interestingly, the stimulation of well 3 resulted in approximately two times as many microseismic events as well 5. One explanation for this observation is that during the stimulation of well 5, the pore pressure was generally increased in the reservoir, resulting in a lower effective stress holding fractures closed. When well 3 was stimulated, less fluid was required to cause fractures to reach the critical state, thereby resulting in

more abundant but smaller magnitude microseismicity and a larger overall  $b$ -value.

Recent work on the concept of the seismogenic index (SI) (Shapiro, 2015) has illuminated fluid injection in the context of geology, seismotectonic state, and risk assessment. SI ( $\Sigma$ ) is defined in equation 1 by the following relationship:

$$\Sigma = \lg N_{\geq M} - \lg Qc(t) + bM, \quad (1)$$

where  $N_{\geq M}$  is the number of microseismic events with a moment magnitude larger than an arbitrarily chosen magnitude  $M$  and  $Qc$  is the cumulative pumped volume of fluid, both as a function of time. It is convenient to calculate SI for discrete stimulation stages using the stage-specific microseismic catalog, pumped volumes, stage  $b$ -value ( $b$ , in equation), and  $M_c$ . We chose  $M$  to be equal to  $M_c$  for each stage. Figure 3a shows the MSEEL site in comparison with other fluid injection sites around the world — hydraulic fracturing (HF)-related and non-HF-related (geothermal, waste disposal, and science). A lower SI indicates a lower overall risk of inducing nuisance seismicity. The MSEEL site lies in the upper half of measured SIs for hydraulically fractured hydrocarbon reservoirs, but it is still less seismogenic than most other fluid injection settings. Figure 3b shows the time series of the SI and  $b$ -value through 21 stages of stimulation at well 5, and Figure 3c shows the SI versus  $b$ -value from 21 stages at well 3. The average SI for well 5 is slightly higher than that of well 3 ( $-4.20$  versus  $-4.51$ ), agreeing with the earlier assessment of well 3 being less than a lower effective stress state due to the earlier stimulation of well 5, resulting in a higher  $b$ -value and lower overall seismogenic potential in well 3.

Given the differences in microseismic abundance,  $b$ -value, and SI between well 5 and well 3, we also examined the microseismic clouds spatially for any apparent differences between the two data sets. When performing spatial assessments of microseismicity, it is important to remove bias from the data cloud by applying an  $M_c$  cutoff. This removes the overabundance of small-magnitude events that tend to cluster near the monitoring location due to improved detection ability. Data become more homogeneously distributed in space and generally become more manageable. We observed relative symmetry in the density of microseismicity about well 5, but an imbalance in well 3, with more microseismicity to the northeast, toward well 5 (Figure 4). This agreed with the conclusion above that the higher pore pressure around well 5 is responsible for a propensity toward abundant small-magnitude microseismicity around well 3 (low SI and high

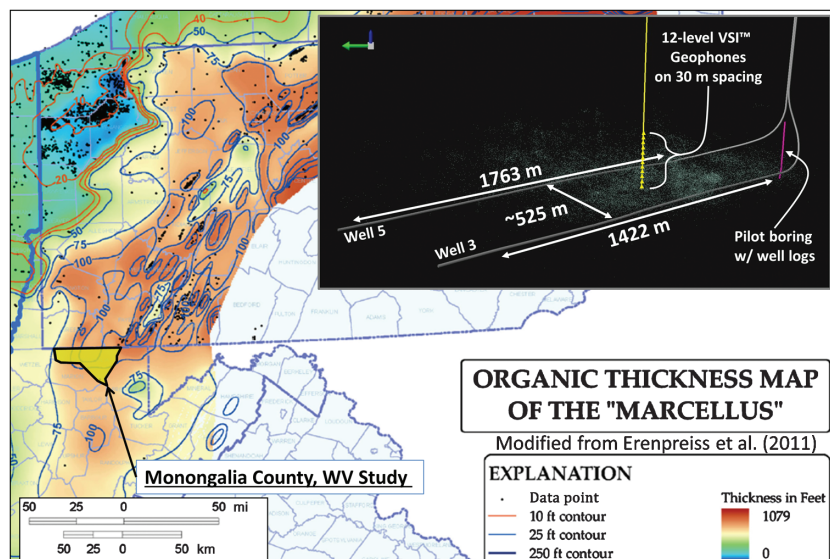


**Figure 1.** Location map, modified from Erenpreiss et al. (2011). Inset is a view of the lateral well geometry and spacing, monitoring well location and configuration, logged pilot hole location and depth, and the microseismic cloud.

b-value). In addition, we observed a distinct change in the alignment of microseismic events occurring during each stage. The average azimuth of alignment, which is a proxy for the orientation of the maximum horizontal compressive stress ( $Sh_{max}$ ), in well 5 is  $N65^{\circ}E$ . The average azimuth in well 3 is  $N77^{\circ}E$ . We calculated this by performing a directional distribution analysis in geographic information systems, fitting a one standard deviation (SD) ellipse to each stage event set. The one SD ellipse contains approximately 68% of the events in the cloud, and the long axis aligns with  $Sh_{max}$ . Figure 4 illustrates this phenomenon of stress shadowing, in which a local change in the alignment of the principal horizontal stresses occurred adjacent to well 3 during the stimulation (pore-pressure increase) of well 5.

In the development of unconventional resources such as the Marcellus Shale, where natural gas is trapped within tight and/or poorly interconnected porosity, direct stimulation of the source/reservoir layer through HF is critical for the recovery of hydrocarbons. Microseismic monitoring provides direct evidence of fracture formation by detecting the resulting seismic events, as documented by Maxwell et al. (2002) and other studies. However, not all of the hydraulic energy transferred downhole is applied to the task of creating fractures in the zone of interest. Much of this energy is lost to heat, fluid energy dissipation, and aseismic deformation (Lee et al., 1991; Boroumand and Eaton 2012). Furthermore, most of the microseismicity occurs outside of the zone of interest. The inefficiency described above should be accounted for when using microseismic data as a measure of stimulation. A too-simplistic approach in which abundant microseismicity should correspond to high hydrocarbon production can lead to over- or underestimates of production. However, the distribution of microseismicity over a vertical span that includes four distinct shale units presents the opportunity to examine the relationship between the rock mechanical properties and the microseismic characteristics. Roche and van der Baan (2015) perform similar work in which they investigate the effect of in situ stress, pore pressure, lithologic layering and coupling, and geomechanical rock properties on the distribution and characteristics of microseismicity at two HF sites.

## Methods

We relied heavily on magnitudes in this approach, and we briefly describe how they are calculated. In this study, a contractor used seismic displacement

to determine the source magnitude. Velocity-based 3C observations were processed and integrated with respect to time to give 3C observations of event displacement. After filtering, the spectrum fitting method (Abercrombie, 1995), was used for the computation of source parameters, including magnitude. Attenuation-corrected models using Brune (1970) and Boatwright (1978, 1980) methods allowed the estimation of the low-frequency limit ( $\Omega_0$ ) and frequency corner ( $f_c$ ) to be independently determined for each receiver, which are then averaged for each event. These estimates were incorporated into the calculation of the seismic moment, which is associated with an event in the catalog that we used in our analysis. This microseismic catalog was a beginning point for our analysis. To compare directly properties of the microseismic catalog such as event magnitude and event count to the geophysical well logs acquired in the vertical pilot well, the microseismic cloud was sampled using a 5 ft vertical window (black rectangular box in Figure 5a) that was advanced through the microseismic cloud at the same interval and elevation as the well logs. This novel approach of moving-average sampling of microseismic attributes

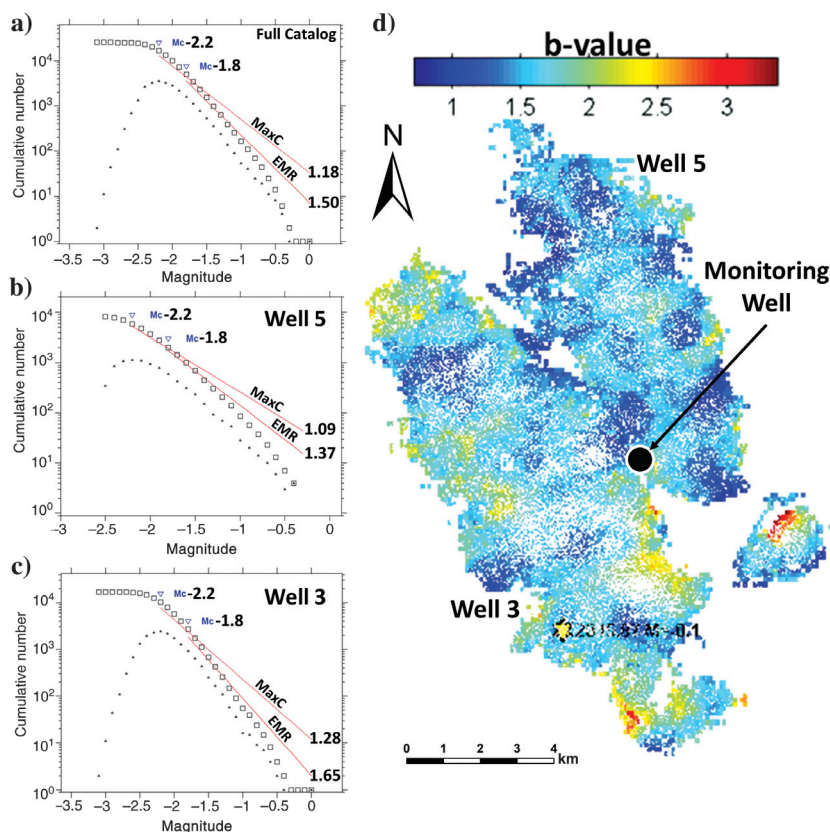


**Figure 2.** (a) The seismogenic b-value of the entire microseismic catalog, (b) well 5 only, (c) and well 3 only, corresponding to the EMR and maximum curvature methods of calculating the completeness magnitude. (d) A depth slide through a 3D b-value map showing the microseismic monitoring well location and the positions of the stimulated wells. The moving b-value was calculated with events inside of a 50 m search radius around each cell, with the added condition that there be a minimum of 20 microseismic events with magnitudes greater than the completeness magnitude.

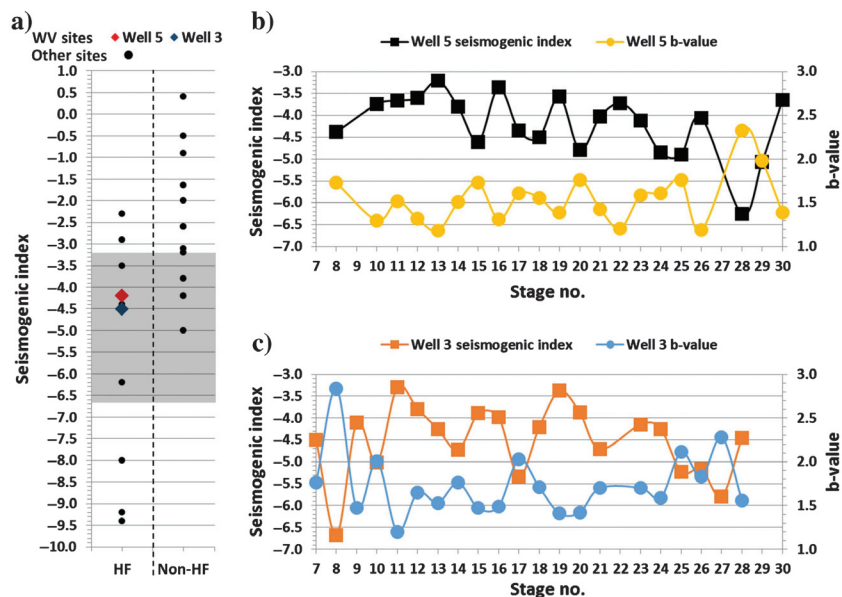


**Figure 3.** (a) The SI of the MSEEL HF site compared with other HF and non-HF sites, including the Barnett Shale, enhanced geothermal, and wastewater injection sites. The shaded area is the range of SI values at MSEEL. Modified from Shapiro (2015). (b) The stage-by-stage evolution of the seismogenic b-value and the SI at MSEEL, well 5, showing an inverse correlation. As stress increases (b-value decreases), the seismogenic potential increases. (c) The stage-by-stage evolution of the seismogenic b-value and the SI at MSEEL, well 3, also showing an inverse correlation.

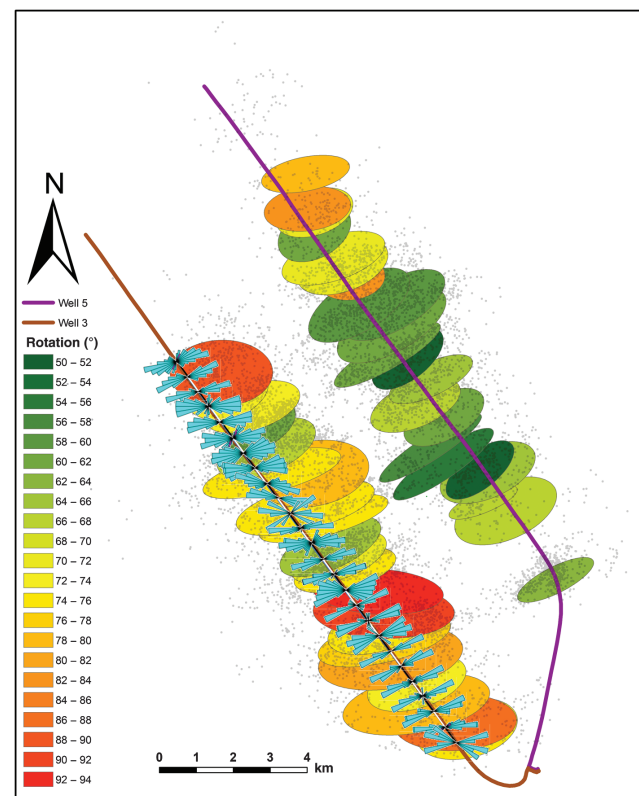


**Figure 4.** One SD directional distribution ellipses fit to microseismic clouds that correspond to each stage of HF. In addition, rose diagrams corresponding to natural fracture orientation and count are overlain on the ellipses.

was developed to create high-resolution microseismic “pseudo” logs that allowed for direct crossplotting and comparison of microseismic versus elastic properties. First, we used ZMAP (Wiener, 2001) to calculate the b-value for the entire microseismic catalog, and the corresponding magnitude of completeness  $M_c$  was then used as a cutoff (Figures 2a and 6), eliminating events with magnitudes too small to be detectable uniformly across the entire site in our analysis (Maxwell, 2012).  $M_c$  is represented in Figure 5a by the sharp cutoff in the microseismic cloud. The moment magnitude of events within the window at each sampling point was averaged to create a moment magnitude pseudolog. The number of events within the moving window at each sampling point was also used to create an event count log. Finally, using the complete data set, we used the slope of the frequency-magnitude distribution (b-value) of microseismicity within a dynamically sized, sliding sample window containing 300 events and create a b-value log. This robust b-value log was then interpolated to

match the well-log sample interval. Figure 5b shows the core set of geomechanical and microseismic logs used in this study.

We examined the variation in average moment magnitude, event count, and b-value, each in a crossplot space consisting of six other variables. These include lambda-rho (LR), mu-rho (MR), gamma, Poisson’s ratio (PR), Young’s modulus (YM), and brittleness. The axes of the crossplot represent LR and MR. PR, YM, and brittleness are represented by isolines of each property within the plot. Gamma is represented as a color gradient from white (low gamma) to black (high gamma). The MR versus LR (MRLR) crossplot forms the foundation upon which these other properties are imposed because they are invariant and form the basic elements of the other moduli. Goodway et al. (2010) illustrate the usefulness of the MRLR space in describing changes in lithology, porosity, elasticity, and fluid content (among other properties) (Figure 7). The pseudologs of microseismic parameters (average moment magnitude, event count, and b-value) are shown in Figures 8, 9, and 10, respectively, as the colored point cloud. The coloring of the point cloud represents the change in value of each parameter. For example, in Figure 8, the maximum average moment magnitude, moving vertically through the microseismic cloud, is  $-1.66$  and the minimum is  $-2.11$ . We consider this crossplot space the most useful in interpreting our attributes. This approach of displaying seven attributes in a single reference plot helps to identify the principal components that drive change in microseismic expression. We

calculated brittleness according to Rickman et al. (2008), in which YM (equation 2) and PR (equation 3) contribute to brittleness individually and together (equation 4):

$$BRIT_{YM} = \left( \frac{YM - 1}{8 - 1} \right) * 100. \quad (2)$$

$$BRIT_{PR} = \left( \frac{PR - 0.4}{0.15 - 0.4} \right) * 100. \quad (3)$$

$$BRIT_{TOTAL} = \frac{(BRIT_{YM} + BRIT_{PR})}{2}. \quad (4)$$

In these equations, it is important to note the YM and PR threshold values that affect the total brittleness calculation. When  $YM = 8$  Mpsi and  $PR = 0.15$ , the resulting material will be “100%” brittle.  $YM = 1$  Mpsi and  $PR = 0.4$  will produce a “0%” brittle material. Reasonable combinations of values are likely constrained within these bounds, resulting in brittleness values of between 0% and 100%. As YM increases, brittleness increases; as PR increases, brittleness decreases.

To reduce detection bias in the microseismic data, we excluded all events with a moment magnitude smaller than the magnitude of completeness ( $-2.2$ ) of the microseismic catalog, as defined by the b-value of the frequency-magnitude distribution (Figure 2; Figure 5a, identified by  $M_c$ ; Figure 6). The location uncertainty ranges from an average of 160 ft in the maximum eigenvector dimension to 42 ft in the minimum dimension. To minimize error, we also excluded all microseismic events with a signal-to-noise ratio  $< 2$ . Stratigraphically, at the project scale, rock units are relatively flat lying and laterally continuous. This was important

in our opinions due to the nature of the sampling and analysis methods being used here, in which well-log properties are treated as laterally applicable and uniform. Because this present study concentrates only on the geomechanical and microseismic properties of organic shale, we excluded any nonshale rocks from the analysis, such as limestone and chert. In an effort to be consistent with a previous study completed in Clearfield County, Pennsylvania (Zorn et al., 2017), we decided to use the same basic log set of  $V_P$ ,  $V_S$ , and  $\rho_B$  (bulk density) as the starting point for all calculations. It is understood that there is uncertainty in the location and magnitude of microseismic events, and also in the assumption that rock layers are flat lying and laterally continuous. We feel that the sampling methods used in this study (sliding/overlapping sampling

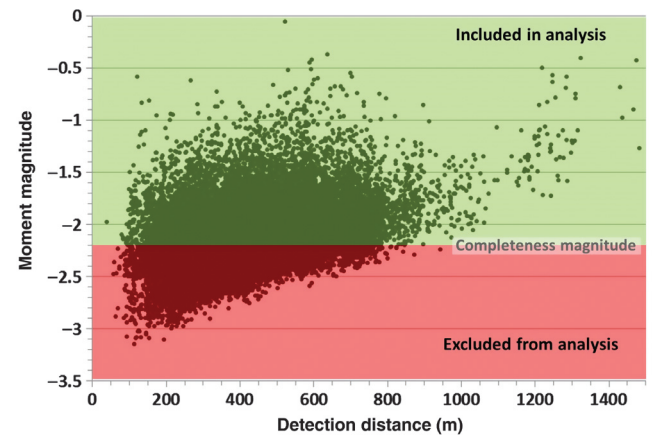


**Figure 6.** Moment magnitude versus detection distance (ft), showing the naturally inclined detection threshold, indicating a decrease in small magnitude detection ability with increased distance. The plot is divided into two panels, based upon a completeness magnitude of  $-2.2$ .

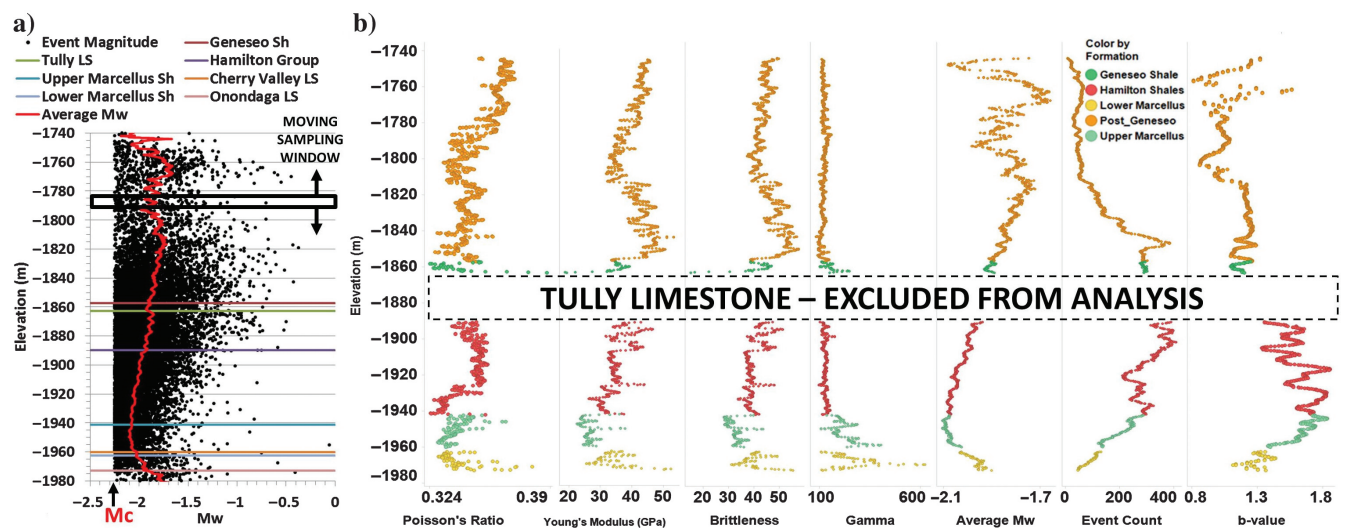


**Figure 5.** (a) The moment magnitude “log” superimposed on the microseismic cloud from which it was calculated. (b) The geomechanical/dynamic moduli logs and microseismic logs forming the foundation of the analyses in this study.

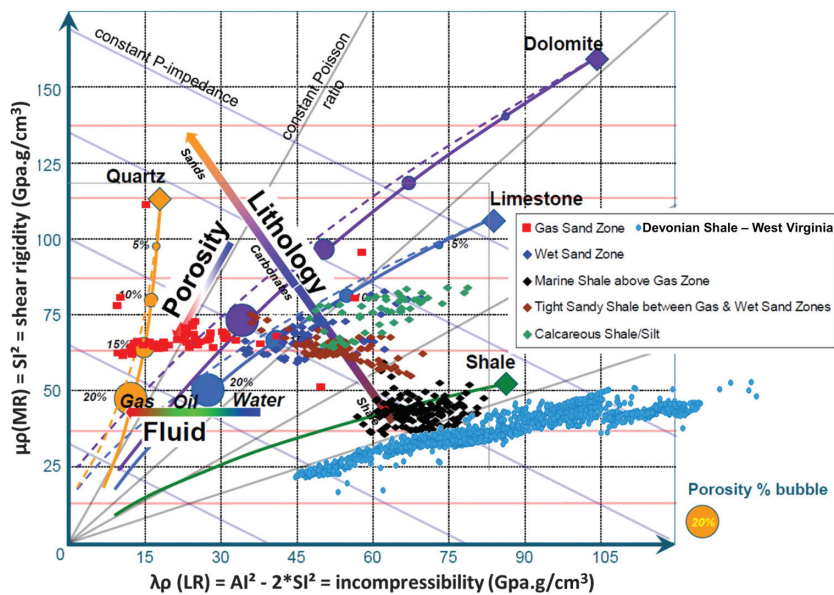


**Figure 7.** The utility of MRLR space, with West Virginia Devonian Shale data superimposed in light blue. Modified from Goodway (2009).

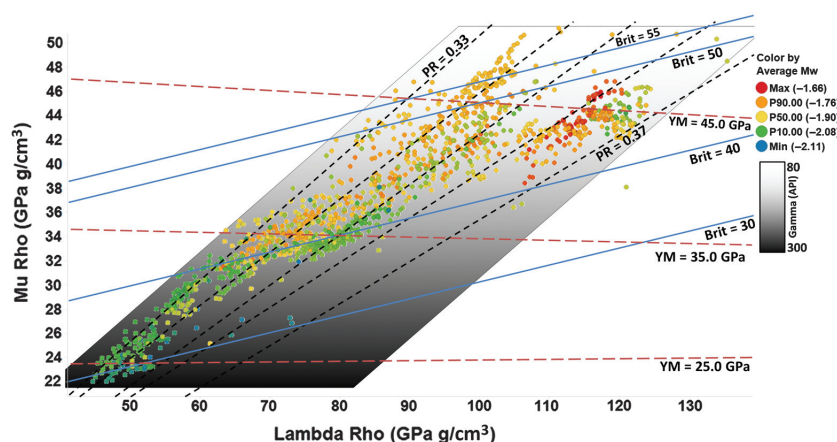


**Figure 8.** The MRLR analysis space colored by average moment magnitude of microseismicity.

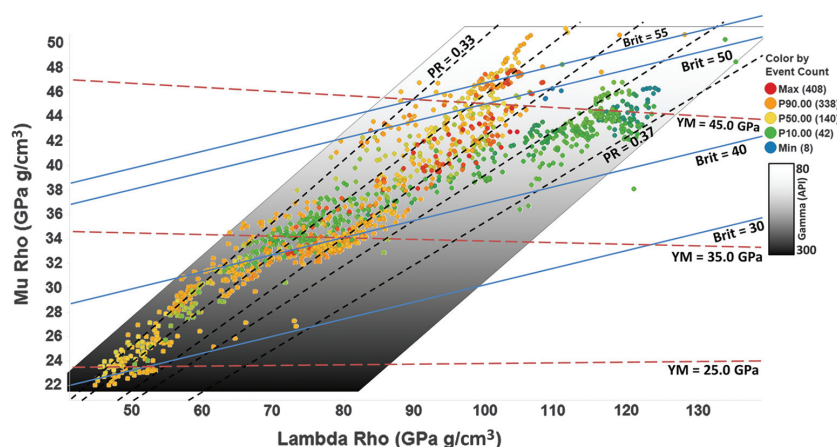


**Figure 9.** The MRLR analysis space colored by microseismic event count.

windows and average magnitudes) are robust enough to soften the effects of this uncertainty.

## Results

To approach the interpretation of this projection of seven different variables, we first examined the data for gradients present at orthogonal angles to isolines of each variable. In examining the data cloud against YM, we saw a direct correlation between increasing or decreasing YM and the presence of relatively large or small moment magnitude events, respectively (Figure 8). In addition, when we examined the data compared with isolines of PR, a relationship emerges in which the smallest magnitude microseismicity generally occurs in the zone of lowest PR and the largest magnitude microseismicity occurs in the zone of highest PR.

Our analysis shows that in this stimulation PR exerts first-order control over the relative abundance of microseismicity (Figure 9). There is a striking juxtaposition of the highest event count next to the lowest event count, within the same zone of YM (>40 GPa). However, the lowest number of events occurs at the highest PR, and microseismicity is most abundant where PR is lowest. Examination of the zone of low PR reveals that there is a secondary gradient in which a combination of high-YM and low-PR conditions will result in more microseismicity than a low-YM/low-PR condition.

The b-value can be interpreted as an indicator of stress condition (Schorlemmer et al., 2005; Goertz-Allmann and Wiemer, 2013). A low b-value indicates that a larger proportion of the event catalog is comprised of larger magnitude seismicity, conceivably a result of higher stress conditions at failure. Conversely, a high b-value (>1) indicates a distribution of seismicity weighted more toward smaller magnitudes as a result of failure in a lower stress condition. In MRLR space, according to Goodway, the state of in situ stress increases with increasing MR and LR. We observed the lowest b-values in the region of the crossplot that generally corresponded to the largest moment magnitudes and lowest event counts (Figure 10). Relating to rock physical properties, low b-values occurred in mid to high YM

and lower gamma (organic content) rocks. Conversely, the highest b-values occurred in rocks with a low YM and the highest organic content. Our interpretation was that the low YM and high organic content would allow internal stresses to be redistributed more readily, discouraging a high stress condition and resulting in a higher b-value.

### Discussion

YM (axial stress/axial strain) is a measure of material stiffness, and PR (axial strain/lateral strain) is a measure of material toughness (Figure 11). Stiffness is the resistance to deformation when stressed, whereas toughness is the resistance to fracturing when stressed. Stiff materials are generally more brittle and prone to fracturing, and resistant to deformation, whereas less stiff materials are tougher. A material that possesses a high PR will likely have a low YM, and vice versa, but there is a natural spread in the possible physical value combinations such that at a given stiffness, materials can be more or less tough, and at a given toughness, materials can be more or less stiff. We interpreted the observed relationships between microseismic properties and elastic properties of organic shale rocks to be the result of these subtle interactions between YM and PR. Of course, there are other variables that undoubtedly influence these relationships, such as existing structures (expulsion features, fractures, faults, or other stress risers), in situ pore pressure, pore shape, permeability/diffusivity, clay and kerogen content, differential stress/closure stress, anisotropy, pumping pressure, rate, volume, and duration. We have tried to address the matter of stress state through the inclusion of b-value analysis. The effect of relative organic content and its relationship with geomechanical and microseismic properties can be seen in the gamma value overlay.

We observed in Figure 8 that the reservoir rocks with the highest PR and YM also host the largest average magnitude microseismicity. These are the toughest and stiffest rocks, meaning that they are resistant to fracturing and resistant to deforming. The inverse is also apparent: The smallest magnitude microseismicity occurs in formation rocks with the lowest YM and the lowest PR.

In the examination of the microseismic event count in the context of geomechanical properties (Figure 9), we observed a first-order gradient in which rocks with the lowest PR host the largest number of microseismic events. A second-order gradient orthogonal to YM indicates that at any value of PR, an increasing YM will cause an increase in the occurrence of microseismicity. No data reside in the low-YM, high-PR zone of the crossplot because this combination of rock mechanical prop-

erties does not exist in this stratigraphic sequence. However, one can extrapolate that in a rock that is highly resistant to fracturing and amenable to deformation, the formation of brittle fractures and associated microseismicity would be a rare occurrence. The zone of maximum event count on the MRLR plot spans the spectrum of YM values but it is focused on the low-PR area, where rocks are more prone to fracturing. It should be noted that in comparing the distribution of moment magnitude and event count in Figures 8 and 9, we observed that the small- to mid-size magnitudes coincide with a greater abundance of microseismicity and that the largest magnitudes coincide with the lowest event counts. This is important because it demonstrates, in an induced microseismic catalog, adherence to frequency-magnitude laws set forth by Gutenberg and Richter (1944).

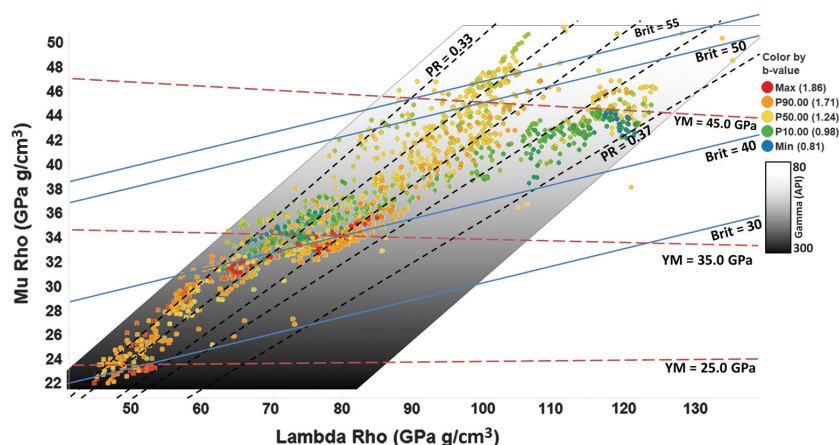


Figure 10. The MRLR analysis space colored by b-value.

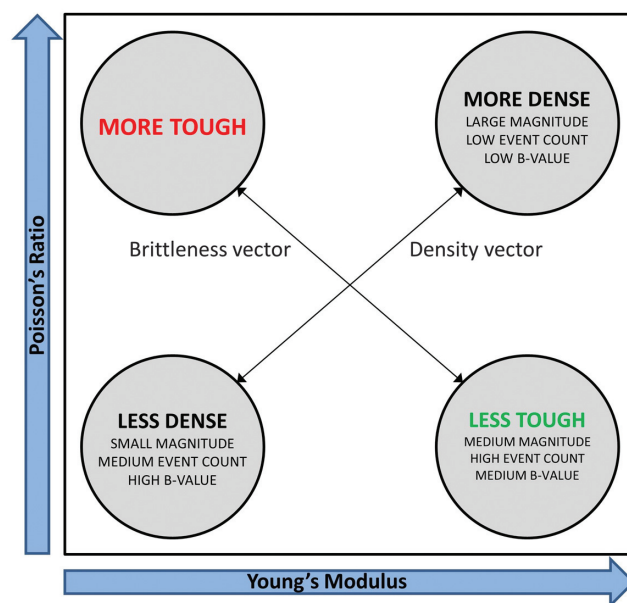


Figure 11. The PR versus YM crossplot space and the distribution of elastic rock properties.

The analysis and discussion of b-value is relevant because it directly relates the magnitude to the abundance of microseismicity, and we have shown that these three seismological attributes are in agreement, i.e., large  $M_w$ →low event count→low b-value, and small  $M_w$ →high event count→high b-value. More importantly, however, is the interpretation of the b-value as an indicator of the in situ stress state at the point of failure. Locally, the state of stress is influenced by the ability of the rock to distribute that stress, which is a function of the shale lithology and microstructure in the area of failure. Figure 10 illustrates that the highest b-values correspond to the lowest values of YM and PR, indicating that an increased ability to deform and/or sustain a fracture in response to stress discourages the development of a high local state of stress. The opposite relationship is also observed, in which the region of highest YM and PR corresponds to the presence of the lowest b-values. In addition, it appears that there is a relationship between the b-value and the gamma value. If gamma is treated as a gross estimator of relative organic or kerogen content, then the most organic-rich shale will be least resistant to deformation in response to stress, and therefore have a tendency to host high b-value microseismicity.

## Conclusion

We have approached a greater understanding of the fundamental geomechanical influences on the microseismic response to HF. Using standard sonic and density well logs, we calculated the dynamic elastic moduli, and we used a novel approach to create comparable microseismic “logs.” A multidimensional MRLR crossplot facilitated a dense and efficient display of meaningful data and uncovered subtle relationships between the elastic properties of organic shale and the seismological attributes of recorded microseismicity. PR exerts a strong influence on the average moment magnitude of seismicity. PR and YM influence the abundance and frequency-magnitude distribution of seismicity. The elasticity of the rock, in the context of toughness and stiffness, directly affects the local in situ state of stress, which in turn, affects the magnitude and abundance of microseismicity.

In terms of importance to energy industry applications, this knowledge can help to refine the concepts of “fracability” and “stimulated” reservoir. Traditionally, more microseismicity translates to “more fracable.” Targeting low-PR rocks will result in increased event counts. In addition, low PR is thought to correlate with higher exploitable organic content and a larger number of existing microfractures and/or expulsion features. However, these events will generally be of the smallest magnitudes. Moment magnitude  $M_w$  is related to the area of the rupture plane and the stress drop at the failure, and the energy release of the failure increases logarithmically on the  $M_w$  scale. There may be some validity to targeting organic shale at the highest end of the PR scale and mid-high YM. Although the event count

will decrease, energy release and area of the failure plane will increase. High PR translates to larger average moment magnitude, and mid-high YM translates to a greater ability to sustain a propped fracture.

Finally, there are myriad other factors that can be less accessible but need to be kept in mind. These may act as additional controls on the microseismic response including existing macro- and microstructure (expulsion features, fractures, faults, or other stress risers), in situ pore pressure, pore shape, permeability/diffusivity, clay and kerogen content, differential stress/closure stress, anisotropy, and pumping pressure/rate/volume/duration. We have established a foundation of understanding from fundamental material properties upon which to build in additional complexity.

## Acknowledgments

We would like to thank the U.S. Department of Energy’s National Energy Technology Laboratory and their industry partners for making this work possible. We would also like to thank *Interpretation* editor H. Zeng and four anonymous reviewers for their valuable comments and suggestions that considerably improved our revised manuscript. We also acknowledge, and are very grateful to, D. Raymer from Schlumberger for explaining in detail the event processing workflow used to create our microseismic event catalog.

## Data and materials availability

Data associated with this research are confidential and cannot be released.

## References

- Abercrombie, R. E., 1995, Earthquake source scaling relationships from -1 to 5 ML using seismograms recorded at 2.5-km depth: *Journal of Geophysical Research*, **100**, 24015–24036, doi: [10.1029/95JB02397](https://doi.org/10.1029/95JB02397).
- Boatwright, J., 1978, Detailed spectral analysis of two small New York state earthquakes: *Bulletin of the Seismological Society of America*, **68**, 1117–1131.
- Boatwright, J., 1980, A spectral theory for circular seismic sources; simple estimates of source dimension, dynamic stress drop, and radiated seismic energy: *Bulletin of the Seismological Society of America*, **70**, 1–27.
- Boroumand, N., and D. W. Eaton, 2012, Comparing energy calculations: Hydraulic fracturing and microseismic monitoring: *GeoConvention 2012: Vision*, doi: [10.3997/2214-4609.20148187](https://doi.org/10.3997/2214-4609.20148187).
- Brune, J., 1970, Tectonic stress and the spectra of seismic shear waves from earthquakes: *Journal of Geophysical Research*, **75**, 4997–5009, doi: [10.1029/JB075i026p04997](https://doi.org/10.1029/JB075i026p04997).
- Erenpreiss, M. S., L. H. Wickstrom, C. J. Perry, R. A. Riley, and D. R. Martin, 2011, Regional organic thickness map of the Marcellus Shale with additional organic-rich shale beds in the Hamilton Group included for New York, Pennsylvania, and West Virginia: Ohio Department of Natural Resources, Division of Geological Survey.

- Goertz-Allmann, B. P., and S. Wiemer, 2013, Geomechanical modeling of induced seismicity source parameters and implications for seismic hazard assessment: *Geophysics*, **78**, no. 1, KS25–KS39, doi: [10.1190/geo2012-0102.1](https://doi.org/10.1190/geo2012-0102.1).
- Goodway, W., 2009, CSM Heiland Lecture: The magic of lamé: Colorado School of Mines — Student Geophysical Society.
- Goodway, W., M. Perez, J. Varsek, and C. Abaco, 2010, Seismic petrophysics and isotropic-anisotropic AVO methods for unconventional gas exploration: *The Leading Edge*, **29**, 1500–1508, doi: [10.1190/1.3525367](https://doi.org/10.1190/1.3525367).
- Gutenberg, B., and C. F. Richter, 1944, Frequency of earthquakes in California: *Bulletin of the Seismological Society of America*, **34**, 185–188.
- Lee, T. S., S. H. Advani, and J. M. Avasthi, 1991, Characteristic-time concept in hydraulic fracture configuration evolution and optimization: *SPE Production Engineering*, **6**, 323–330, doi: [10.2118/19000-PA](https://doi.org/10.2118/19000-PA).
- Maxwell, S. C., 2012, Comparative microseismic interpretation of hydraulic fractures: Presented at the SPE Canadian Unconventional Resources Conference, Paper SPE-162782-MS, doi: [10.2118/162782-MS](https://doi.org/10.2118/162782-MS).
- Maxwell, S. C., T. I. Urbancic, N. Steinsberger, and R. Zinno, 2002, Microseismic imaging of hydraulic fracture complexity in the Barnett shale: Presented at the SPE Annual Technical Conference and Exhibition, Paper SPE-77440-MS, doi: [10.2118/77440-MS](https://doi.org/10.2118/77440-MS).
- Rickman, R., M. J. Mullen, J. E. Petre, W. V. Grieser, and D. Kundert, 2008, A practical use of shale petrophysics for stimulation design optimization: All shale plays are not clones of the Barnett shale: Presented at the SPE Annual Technical Conference and Exhibition, Paper SPE-115258-MS, doi: [10.2118/115258-MS](https://doi.org/10.2118/115258-MS).
- Roche, V., and M. van der Baan, 2015, The role of lithological layering and pore pressure on fluid-induced microseismicity: *Journal of Geophysical Research Solid Earth*, **120**, 923–943, doi: [10.1002/2014JB011606](https://doi.org/10.1002/2014JB011606).
- Schorlemmer, D., S. Wiemer, and M. Wyss, 2005, Variations in earthquake-size distribution across different stress regimes: *Nature*, **437**, 539–542, doi: [10.1038/nature04094](https://doi.org/10.1038/nature04094).
- Shapiro, S., 2015, *Fluid-induced seismicity*, 1st ed.: Cambridge University Press.
- Wiemer, S., 2001, A software package to analyze seismicity: ZMAP: *Seismological Research Letters*, **72**, 374–383, doi: [10.1785/gssrl.72.3.373](https://doi.org/10.1785/gssrl.72.3.373).
- Woessner, J., 2005, Assessing the quality of earthquake catalogues: Estimating the magnitude of completeness and its uncertainty: *Bulletin of the Seismological Society of America*, **95**, 684–698, doi: [10.1785/0120040007](https://doi.org/10.1785/0120040007).
- Zorn, E., R. Hammack, W. Harbert, and A. Kumar, 2017, Geomechanical lithology-based analysis of microseismicity in organic shale sequences: A Pennsylvania Marcellus Shale example: *The Leading Edge*, **36**, 845–851, doi: [10.1190/le36100845.1](https://doi.org/10.1190/le36100845.1).

---

Biographies and photographs of the authors are not available.